Image Cover Sheet

CLASSIFICATION	SYSTEM NUMBER
UNCLASSIFIED	512722

TITLE

Lidar Characterization of Cloud Liquid Water Content and Effective Droplet Diameter

System Number:

Patron Number:

Requester:

Notes:

DSIS Use only:

Deliver to:

REPRINT

EUROPTO® SERIES

Reprinted from

Laser Radar Ranging and Atmospheric Lidar Techniques II

20–21 September 1999
Florence, Italy

SPIE PROCEEDINGS SERIES

Volume 3865

Lidar characterization of cloud liquid water content and effective droplet diameter

Luc R. Bissonnette and Gilles Roy

DREV-Defence Research Establishment Valcartier
2459, Pie XI Blvd. North, Val-Bélair, Québec, Canada, G3J 1X5
Tel.: +418-844-4437 • *Fax*: +418-844-4511 • *E-mail*: luc.bissonnette@drev.dnd.ca

ABSTRACT

Supercooled cloud and precipitation water droplets constitute a safety hazard to aviation. Concerned agencies are funding research on methods of remotely sensing the icing potential of such clouds and precipitation. The parameters needed are the temperature, the liquid water content (LWC) and the average droplet size. We report here on preliminary results obtained with a multiple-field-of-view (MFOV) lidar in an experimental program carried out at Mount Washington during April 1999. The MFOV technique consists in the measurement of the forward multiple scattering contributions to lidar returns coupled with a solution method that makes use of this additional information to calculate the extinction coefficient and the effective droplet diameter as the dependent functions, and the LWC as a by-product. The paper describes the MFOV retrieval method and gives sample results obtained in the Mount Washington experiment. The retrieved solutions demonstrate the lidar capability of remotely sensing droplet size and LWC profiles of clouds and precipitation. Solution accuracy is determined to be 30-40% but the analysis of the data from all fielded sensors will be needed to validate these numbers.

Key words: Lidar, multiple scattering, clouds, precipitation

1. INTRODUCTION

Lidar is one of the first application that has quickly followed the invention of the laser.[1] The principle is the same as for radar but the comparatively very short wavelengths of laser sources have opened the way to new application fields. The lidar has been successfully used to retrieve profiles of atmospheric constituents and trace gases, to monitor pollution, to detect clear air turbulence, etc. Major projects are currently underway for making global wind measurements which is possible with a lidar because it can still work at very low aerosol loadings. Recently, a need has been expressed for the remote detection of regions of supercooled cloud and precipitation water droplets responsible for in-flight icing of aircraft. The lidar appears as a valid candidate for this task but, at the high particulate concentrations encountered in such conditions, extinction creates retrieval difficulties because of nonlinearity and multiplicity of unknowns.[2] Indeed, single scattering lidar solution methods have had mixed success at quantifying parameters of dense aerosols. The icing detection problem is therefore a challenge to conventional lidar methods.

For a number of years, we have been working on a multiple-field-of-view (MFOV) detection technique to capture and angularly resolve the multiply forward scattered photons.[3,4] Multiple scattering in lidar has been the subject of numerous studies.[5] The direct problem is well understood and modeled but inversion methods for the quantitative retrieval of the information contributed by multiple scattering are only emerging. We are actively pursuing this goal with the MFOV lidar.[6–9] Detection of icing conditions is particularly well suited to the MFOV method because the responsible clouds are dense enough to produce measurable multiple scattering and the droplets are in the right size range to be resolved at the lidar wavelength. Consequently, the invitation to participate in a coordinated experimental program designed to assess icing detection technologies was very much welcomed. The project was a unique opportunity to gain access to quality validation data and to evaluate the MFOV lidar as a potential remote sensor of icing conditions.

2. MFOV LIDAR TECHNIQUE

The multiple field-of-view (MFOV) lidar technique is designed to measure the multiple scattering contributions to lidar returns. A first system[3] was built a number of years ago and used by Hutt *et al.*[4] to demonstrate the principle.

Part of the EUROPTO Conference on Laser Radar Ranging and Atmospheric Lidar Techniques II
Florence, Italy • September 1999
SPIE Vol. 3865 • 0277-786X/99/$10.00

2.1. Lidar System

The system currently in use by our group has been described elsewhere.[10,11] In short, it consists of a linearly polarized Nd:YAG laser operating at a repetition frequency of 100 Hz. The pulse energy, pulse length, beam diameter, and beam divergence are 70 mJ, 12 ns, 25 mm and 0.5 mrad, respectively. The receiver main optics is a 200-mm diameter off-axis parabolic mirror of a focal length of 760 mm.

The characteristics given above are rather conventional. What makes our lidar special is the capability of changing the receiver field of view (FOV) at the repetition frequency of the laser source. This is accomplished by means of a rotating 125-mm diameter aluminized glass disk with irises or rings of different sizes etched on the periphery. The disk is positioned in the image plane of the main mirror in such a way that the circle drawn by the centers of the irises or rings lies on the center of the imaged laser spot. The laser Q-switch is slaved to the rotation velocity of the disk to insure that the center of the individual irises or rings is aligned with the system optical axis at the time when the backscattered returns reach the receiver. The disk is considered frozen for the duration of the backscattered signal. For our system, the useable signal lasts no more than 20 μs during which time the irises or rings move less than 2% of the imaged spot size of singly scattered returns. Thus, for our application of resolving the angular beam spread of the multiply scattered contributions, the approximation is justified.

The disk used for the measurements reported in this paper has 32 irises defining FOVs between 0.1 and 12 mrad, full angle. Of these, only 16 are applicable to retrieval because the 16 smallest FOVs are less than the beam divergence. The small FOVs are used for characterizing the laser beam profile and for alignment purposes. Whatever the FOV sequence selected for retrieval, it repeats itself every 32/100 s. Therefore, the probed medium must not fluctuate on the whole at frequencies greater than $\sim$ 3 Hz. All clouds and precipitation recorded during the experiment reported here did satisfy this requirement most of the time.

The radiation passing through the disk irises is re-collimated, split into perpendicular and parallel polarization components with respect to the linearly polarized outgoing laser pulse, and finally re-imaged with a magnification of 0.3 on 3-mm diameter avalanche photodiode detectors. The electronic signal is then log-amplified to compress its dynamic range, and digitized (8 bit) at a selectable frequency of 12.5, 25, 50 or 100 MHz. The maximum achievable dynamic range is 4.5 decades and the digitization frequencies define range bins of 12, 6, 3 and 1.5 m, respectively. The intrinsic lidar spatial resolution based on pulse length is 1.8 m.

Both the outgoing laser pulse and the backscattered radiation pass through a 350mm$\times$225mm elliptical, 45-degree incidence plane mirror that can be rotated about a horizontal axis. This allows pointing the lidar at any elevation angle in a fixed vertical plane.

A typical MFOV measurement consists of a burst of 1000 lidar pulses at 100 Hz with the FOV disk continuously rotating. The bursts, therefore, last 10 s and contain 1000/32 = 31 complete sequences of usable FOVs. The retrieval method needs only one of these sequences. However, to smooth out fluctuations, we normally integrate over a selectable number of sequences before starting the calculations. The number of sequences used depends on the rapidity with which the cloud or precipitation evolves during the 10-s duration of the bursts.

2.2. Solution Method

The object of the solution method is to retrieve the cloud or precipitation extinction coefficient and average droplet size, and from there the liquid water content. A main characteristic of the proposed method is the exploitation of the information contained in the multiple scattering contributions to the lidar returns. As described in the preceding paragraphs, the MFOV receiver provides a direct measure of these contributions. The retrieval technique proposed here is an evolving solution method that still needs refinements and extensive validation. Earlier versions have been reported elsewhere.[7,12] We will recall in this paper only the basic principles and assumptions.

Figure 1a shows the raw MFOV returns from a cloud layer at 400 m from the transceiver. Eight curves are plotted corresponding to eight FOVs ranging from 1 to 12 mrad. If there were no multiple scattering, all eight signals would be the same since the FOVs are all greater than the beam divergence. The observed additional contributions at the larger FOVs result from forward scattered photons that remain within those FOVs. It is evident from Fig. 1a that this effect can be substantial. Conventional lidar solution methods ignore these contributions and thus require small receiver FOVs. Here, on the contrary, our goal is to make use of these additional contributions.

As illustrated in Fig. 1a, there is initially no significant difference between the FOVs except for some fluctuations

at very low signal levels and within a weak layer below the main cloud where the returns vary rapidly with range and presumably between FOV recordings. In other words, backscatter is still dominated by singly backscattered photons at cloud base. However, as the pulse penetrates further into the cloud, more and more forward scattered photons are being produced that give rise to backscattering from an increasingly wider region about the laser axis. This is evidenced by the wide-FOV signals that progressively grow larger relative to the smallest FOV return. In Fig. 1b, we have plotted from the data of Fig. 1a the relative signal increase with FOV for selected altitudes. The combined results of Fig. 1 thus show that both the strength and the FOV scale of the multiply scattered lidar returns depend on penetration distance and optical depth. Also, as will be discussed later, the FOV scale is linked to droplet size. It is in fact those relations that we try to invert to derive the cloud extinction coefficient and average droplet diameter at the range resolution defined by the laser pulse length.

As is well known, inverse problems are mathematically ill posed problems, especially in complex situations such as multiple scattering. Our approach is semi-empirical. It lacks the mathematical rigor of formal constrained inversion methods but it requires only modest computation resources and gives consistent results in most applications.

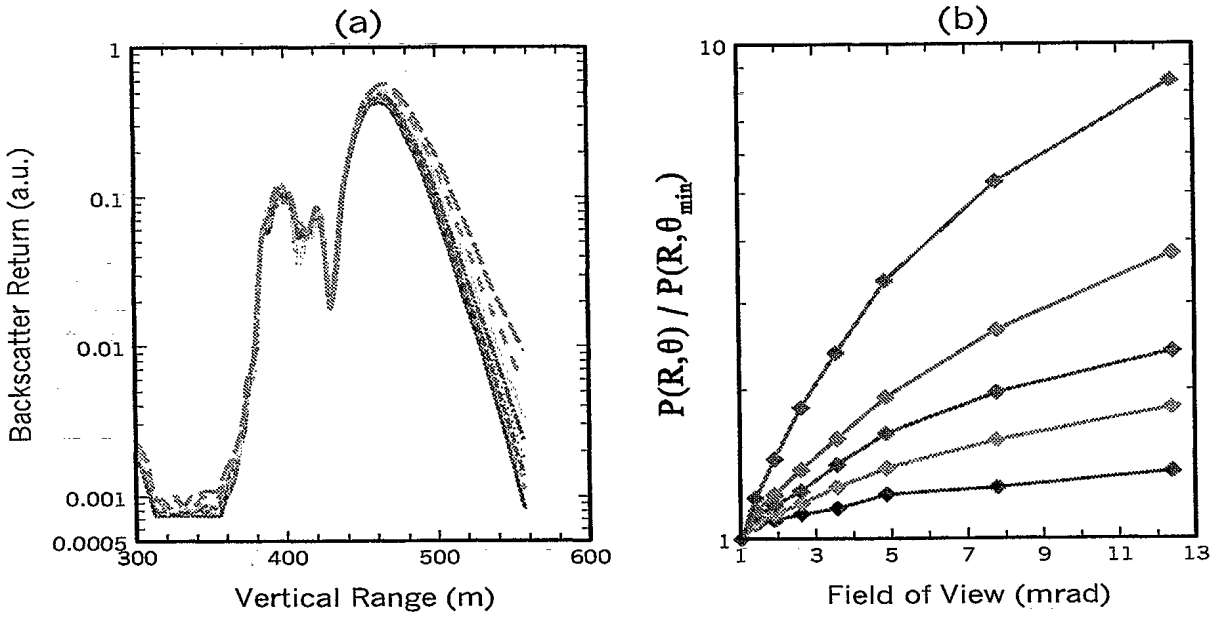

Figure 1. MFOV lidar signals measured vertically from a cloud at 400 m height above ground. a: returns as functions of vertical range for FOVs of 1.03, 1.41, 1.92, 2.62, 3.57, 4.88, 7.78 and 12.4 mrad in order of increasing signal. b: normalized FOV dependence of measured returns at altitudes of 465, 485, 500, 525 and 550 m in order of increasing signal. θ is FOV and θ_{min} is smallest FOV in Fig. 1a.

Droplet Diameter: The droplet diameter at each range bin is determined from the experimentally calculated FOV scale of curves such as plotted in Fig. 1b. Multiply scattered lidar returns are essentially a measure of forward scatterings. This is valid in the approximation that the radiation collected by the receiver is the sum of small-angle forward scatterings in both the forward and backward legs of the photon trajectories plus a single backscattering at

an angle close to 180 degrees. This condition requires that the FOV footprint be much less than the photon mean free path between scatterings, and it insures that there is no substantial pulse stretching or that range resolution based on time of flight is preserved. Backscatter plays a role in the FOV dependence of the measured returns but it is neglected in the small-angle approximation since all backscatterings occur at angles close to 180 degrees. As a consequence, the FOV scale of the measured returns can be simply and directly related to the forward angular spread of the outgoing beam caused by scattering. The small-angle forward scattering conditions were satisfied for all cases reported here.

The principle of resolving the forward scattering peak to determine droplet or aerosol particle size is used in many particle spectrometer designs. It has also been used successfully by Roy *et al.*[8,9] to retrieve droplet size distributions in the same lidar configuration as used here . The physical basis is that forward scattering by particles large enough compared with the radiation wavelength is mostly caused by diffraction, which implies that the resulting angular spread is inversely proportional to the particle size. Here, we follow the same principle with the added difficulty of having to take into account the extra spread caused by multiple forward scatterings. Consequently, we do not attempt to retrieve the full size distribution but only a mean value. We propose without demonstration the following semi-empirical model to relate the diffraction-induced angular scale θ_d to the measured FOV scale θ_m:

$$\theta_d^2(R) \;=\; \left[R^2\,\theta_m^2(R) \;-\; R_b^2\,\theta_m^2(R_b)\right] \,/\, (R - R_b)^2\,, \tag{1}$$

where θ_d is the width of the diffraction peak of the single scattering phase function, θ_m is the FOV scale of the measured returns, e.g. of curves such as drawn in Fig. 1b, R is the current range, and R_b is the range one optical depth upstream. The diffraction width θ_d is approximated by[6]

$$\theta_d \;\simeq\; 1.7\,\frac{\lambda}{\pi\,d}\,, \tag{2}$$

where λ is the lidar wavelength, d is the average effective droplet diameter defined as the ratio of the third to the second order moment of the size distribution, and 1.7 is an empirical constant. Hence, d can be calculated at each range R by substitution of eq. 2 for θ_d in eq. 1.

Extinction Coefficient: The solution for the extinction coefficient begins at the range position R_{ms} where the relative multiple scattering strength, measured for example by the ratio of the largest to the smallest FOV returns, reaches a preset threshold, say 1.05. For the data of Fig. 1, this occurs near 465 m. At that multiple scattering level, a first order or single forward scattering model can be used to estimate the return. For instance, we have from Ref. 6

$$\frac{P(R,\theta)}{P_{ss}(R)} \;\simeq\; 1 \,+\, 0.86\,\delta\,\tau\left\{\sqrt{\pi}\,\frac{\theta}{\theta_d}[1 - \Phi(\theta/\theta_d)] \,+\, [1 - \exp(-\theta^2/\theta_d^2)]\right\}\,, \tag{3}$$

where $P(R,\theta)$ is the multiply scattered return from range R and within FOV θ, P_{ss} is the conventional single scattering lidar expression, δ is the ratio of the backscatter coefficient averaged over the angular range θ_m about 180 degrees to the coefficient at exactly 180 degrees ($\delta \simeq 0.7$), $\tau = \int_0^R \alpha(r)dr$ is the optical depth at R, α is the extinction coefficient, and Φ is the error function. P_{ss} is given by

$$P_{ss}(R) \;=\; C\,\frac{\beta(R)}{R^2}\,\exp[-2\tau(R)]\,, \tag{4}$$

where C is the system constant and β is the backscatter coefficient at exactly 180 degrees.

We split the solution sequence for the extinction coefficient $\alpha(R)$ into two main stages: first for $R \le R_{ms}$ using multiple scattering to obtain a boundary value and single scattering for the solution itself, and second for $R > R_{ms}$ using direct multiple scattering calculations. Details are given below.

The solution for $R \le R_{ms}$ begins by fitting eq. 3 to the multiple scattering strength $P(R_{ms},\theta)/P(R_{ms},\theta_{min})$ measured at the threshold range R_{ms} where $P(R_{ms},\theta_{min})$ estimates $P_{ss}(R_{ms})$. We thus obtain $\tau(R_{ms})$ and $\theta_d(R_{ms})$. Then, we solve the single scattering lidar equation 4 for all ranges $R \le R_{ms}$ using $\tau(R_{ms})$ in lieu of a boundary value as described by Kunz.[13] That solution is valid because we know from measurements that multiple scattering is small in that region.

Next, we use the solution just derived to determine the system constant C as a prerequisite for the calculation of $\alpha(R > R_{ms})$. Since Kunz's solution is independent of C, we simply derive C by substituting in eq. 4 the retrieved extinction coefficient $\alpha(R_{ms})$, the optical depth $\tau(R_{ms})$ and $P(R_{ms}, \theta_{min})$ as a valid estimate of $P_{ss}(R_{ms})$. There remains to relate β to α. This we do by making Mie calculations based on the effective droplet diameter obtained earlier and the assumption of a modified gamma function for the droplet size density distribution. This completes the determination of C. To proceed further and compute $\alpha(R > R_{ms})$, we need an expression for the multiply scattered lidar return $P(R, \theta)$. We propose the following general form:

$$P(R,\theta) \;=\; \alpha(R)\,\frac{C}{R^2}\,\frac{\beta(R)}{\alpha(R)}\,\exp[-2\tau]\,M(\tau,R,\theta)\,, \tag{5}$$

where M is the multiple scattering correction to the single scattering lidar equation. M is a function of optical depth, range and FOV; its actual form depends on the multiple scattering model used. The constant C is the same as in eq. 4. We therefore have all the needed inputs to calculate $\alpha(R)$ by direct substitution in eq. 5. The functions τ and M are computed from the α and d solutions already determined at all ranges less than R, and the ratio β/α is evaluated from d as explained above. Both α and d solutions are run in parallel because they are interdependent through M and β/α. Since τ and M are functions of $\alpha(R)$, there remains to update their values up to current range R, which is easily accomplished by iterating the process.

For the results reported here, we have used the model of Ref. 6 to calculate the function M but any other model would be suitable, including Monte Carlo's. One advantage of the method is that it replaces the difficult problem of inverting the complex nonlinear multiple scattering lidar equation into the much simpler direct calculation of the multiple scattering function M. It may be objected that direct substitution in eq. 5 will lead to instabilities because of the exponential function $\exp(-2\tau)$. The presence of M which grows with τ greatly minimizes this problem. Actually, we further improve on this by using not eq. 5 but rather

$$\frac{P^2(R,\theta_{max})}{P(R,\theta_{min})} \;=\; \alpha(R)\,\frac{C}{R^2}\,\frac{\beta(R)}{\alpha(R)}\,\exp[-2\tau]\,\frac{M^2(\tau,R,\theta_{max})}{M(\tau,R,\theta_{min})}\,, \tag{6}$$

where θ_{max} and θ_{min} are the largest and smallest FOVs, respectively. The ratio $M^2(\tau, R, \theta_{max})/M(\tau, R, \theta_{min})$ compensates almost completely for the exponential fading. As a result, we have seldom experienced instabilities.

Liquid Water Content: The liquid water content LWC of a cloud made up of spherical droplets is defined by

$$\mathrm{LWC} \;=\; \frac{4\pi}{24}\,\rho \int_0^\infty \frac{\mathrm{d}N}{\mathrm{d}x}\,x^3\,\mathrm{d}x\,, \tag{7}$$

where ρ is the density of liquid water and $\mathrm{d}N/\mathrm{d}x$ is the droplet diameter density distribution function. Similarly, the extinction coefficient is given by

$$\alpha \;=\; \frac{\pi}{4}\int_0^\infty \frac{\mathrm{d}N}{\mathrm{d}x}\,Q_e(x,\lambda)\,x^2\,\mathrm{d}x\,, \tag{8}$$

where Q_e is the extinction efficiency function. For most clouds and rain conditions experienced, the droplet diameters are such that $Q_e \simeq 2$ at the lidar wavelength of 1.06 μm. Ratioing eqs. 7 and 8 and using $Q_e = 2$, we have

$$\frac{\mathrm{LWC}}{\alpha} \;=\; \frac{1}{3}\,\rho\,\frac{\int_0^\infty \frac{\mathrm{d}N}{\mathrm{d}x}\,x^3\,\mathrm{d}x}{\int_0^\infty \frac{\mathrm{d}N}{\mathrm{d}x}\,x^2\,\mathrm{d}x}\,. \tag{9}$$

Since the effective droplet diameter d is defined as the ratio of the third to the second order moment of the size distribution, we thus have the following simple relation to calculate LWC from the lidar solutions $\alpha(R)$ and $d(R)$:

$$\mathrm{LWC}(R) \;=\; \frac{1}{3}\,\rho\,\alpha(R)\,d(R)\,. \tag{10}$$

Actually, we use

$$\mathrm{LWC}(R) \;=\; \frac{2}{3 < Q_e >}\,\rho\,\alpha(R)\,d(R)\,, \tag{11}$$

where the average $< Q_e >= \int(\mathrm{d}N/\mathrm{d}x)Q_e(x,\lambda)x^2\mathrm{d}x/\int(\mathrm{d}N/\mathrm{d}x)x^2\mathrm{d}x$ is easily calculated from the Mie efficiency factor $Q_e(x,\lambda)$ and the assumption of a modified gamma function parametrized by d for $\mathrm{d}N/\mathrm{d}x$ as was done earlier for estimating β/α.

Sample Solutions The inversion results calculated from the data of Fig. 1a are plotted in Fig. 2. On the left panel are the retrieved extinction coefficient and effective droplet diameter profiles, and on the right panel the corresponding liquid water profile. The lidar was pointed vertically for these measurements.

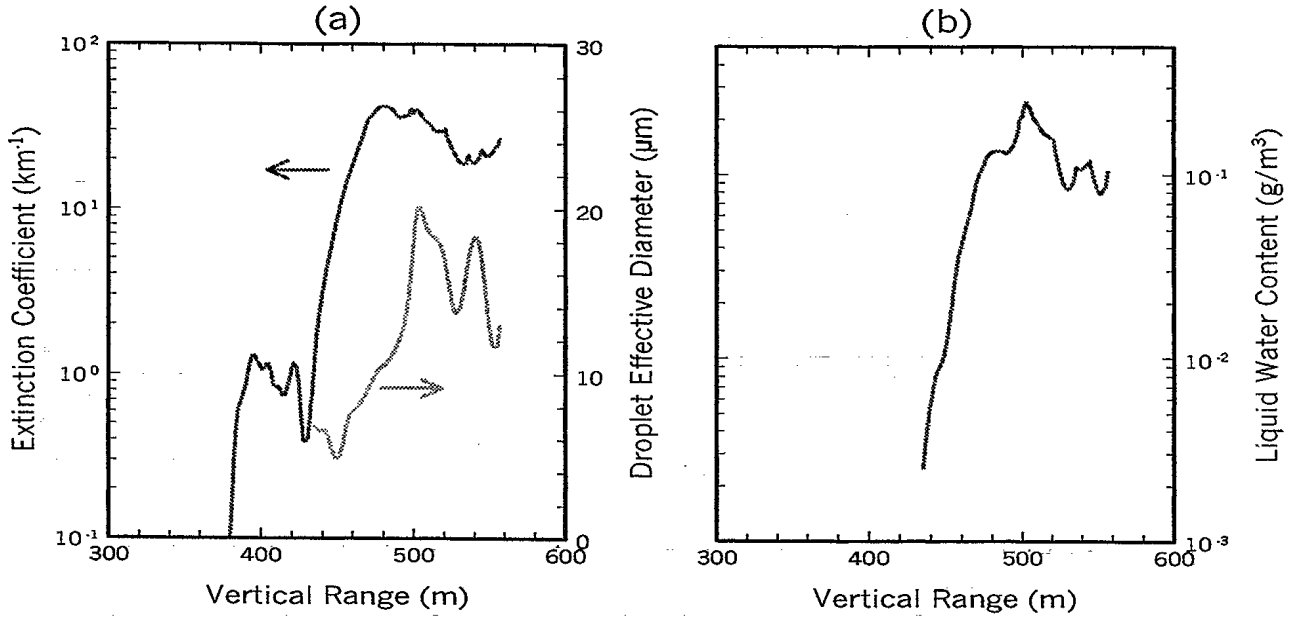

Figure 2. Inversion solutions derived from the data of Fig. 1a. a: extinction coefficient and effective droplet diameter as functions of vertical range. b: liquid water content profile derived from the extinction and diameter solutions.

The extinction profile reveals a sublayer about 40 m deep with an extinction coefficient of about 1 km^{-1}. The main layer has a very sharp boundary where the extinction jumps from less than 1 to $\sim$ 40 km^{-1} in just 30 m. The extinction coefficient then fluctuates between 20 and 40 km^{-1} for the remaining 100-m range of measurable lidar signal. The solution ends where the smallest FOV return drops to the system detection threshold.

The diameter solution begins above the sublayer because there is not enough forward scattering below for reliable calculations. The droplet size increases at cloud base, as expected, before settling down with obvious fluctuations in the 10 to 20 μm range. Whether these oscillations are real or not cannot be ascertained for the moment but, on the average, the values make sense for this type of clouds.

The liquid water content varies between 0.1 and 0.25 g/m^3 over the probed cloud depth. Again, we have no detailed profile data to compare with at this early stage of the analysis but the retrieved values are certainly within expectations. We will discuss solution accuracy at greater length in the discussion section after more systematic retrieval results have been presented.

3. EXPERIMENTAL RESULTS

3.1. MWISP Experiment

The Mount Washington Icing Sensors Project (MWISP) experiment took place at Mount Washington, New Hampshire from 1 to 29 April 1999. The MFOV lidar was co-located with meteorological radars 3.9 km west and at an altitude of about 1000 m below the mountain summit. The observatory at the summit was instrumented with a host of point sensors for characterizing the cloud and precipitation microphysics. Coordinated measurements were carried out during most overcast conditions which amounted to a total of 19 significant measurement periods.

The full experiment will be described elsewhere. At the time of writing, most groups are still busy validating their data. No systematic analysis has begun yet. The aim of this paper is to report on preliminary lidar results.

3.2. Cloud and Precipitation Structure

Raw lidar backscatter and depolarization measurements provide vivid pictures of the cloud/precipitation structure and phase. Up to some penetration depth, the backscatter strength is proportional to droplet density and thus gives a good indication of spatial and temporal density fluctuations. On the other hand, the depolarization ratio, defined as the ratio of the perpendicular to the parallel polarization components, constitutes a simple estimate of the water or crystal phase composition of the probed clouds or precipitation. Some care must be exercised, however, in interpreting the backscatter results because of the inverse range squared dependence and the eventual extinction by scattering and absorption. Being a ratio, depolarization does not suffer from these effects.

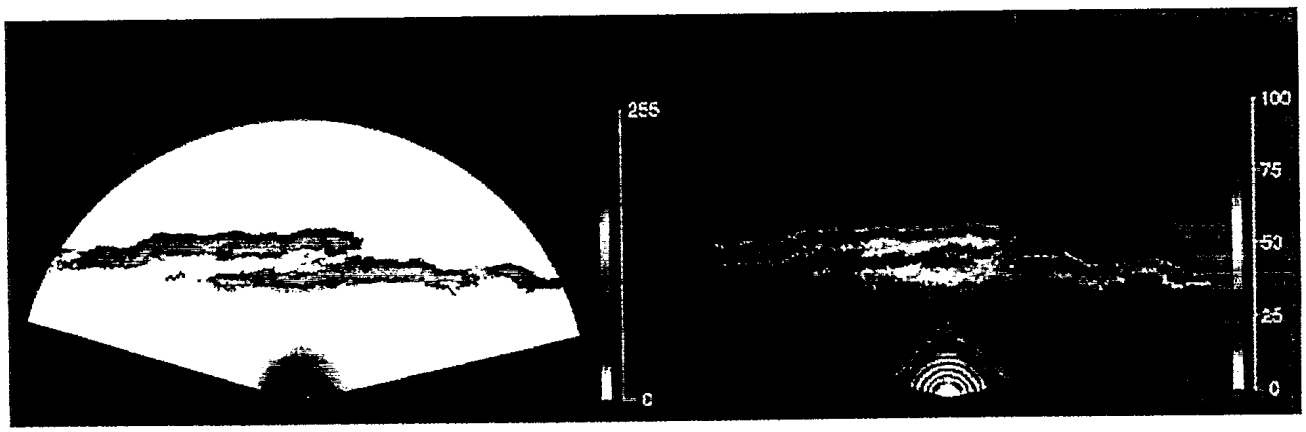

Figure 3. Color-coded elevation-versus-range backscatter (left) and depolarization ratio (right) maps obtained on 7 April 99 at 11:20 UTC. Scan plane is oriented east-west with the east or mountain side to the right. Radius of scan is 1.2 km. Backscatter scale is logarithmic and in arbitrary units; depolarization scale is %. Extended regions of 100% depolarization are default values for negligible signal strength.

We have made several measurements during MWISP to obtain snapshots of the cloud and precipitation structure between the mountain and the valley by performing constant speed elevation scans. The scan plane was vertical and directed east-west, i.e. in the line-of-sight direction to the summit observatory. For these measurements, we have kept the FOV to a constant value of 4 mrad. The time required to complete a scan from 15 to 165 degrees in elevation was 80 s.

A first result is depicted in Fig. 3 which shows maps of the backscatter and depolarization ratio as functions of elevation angle and radial range in the case of an overcast sky with no precipitation. Backscatter indicates a rather structured cloud base with two distinct layers above the lidar site. The white-to-light-blue color of the depolarization map, i.e. low depolarization values, means that the cloud is pure water. In Fig. 4, we show the same plots but for a rain event. The backscatter still confirms the presence of a well defined cloud base, although jagged and of variable height, but depolarization shows a more diffuse transition from cloud to rain because rain also causes little depolarization. Large rain drops are generally squashed by their fall velocity and should produce more depolarization

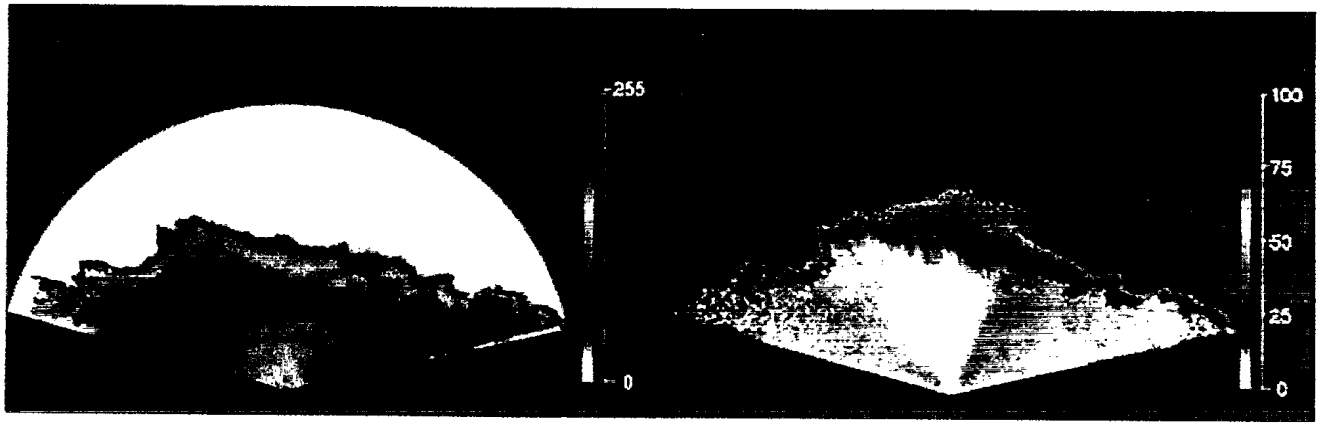

Figure 4. Color-coded elevation-versus-range backscatter (left) and depolarization ratio (right) maps obtained on 14 April 99 at 20:28 UTC. Scan plane is oriented east-west with the east or mountain side to the right. Radius of scan is 1.2 km. Backscatter scale is logarithmic and in arbitrary units; depolarization scale is %. Extended regions of 100% depolarization are default values for negligible signal strength.

away from the vertical. There is some evidence of this in Fig. 4 but the effect may be masked by depolarization caused by the scanning mirror. Further calibration tests will need to be made on scanner-induced depolarization.

The next case illustrated in Fig. 5 is for a light snow fall. As in the previous figures, the backscatter plot still reveals the cloud layers but not so clearly at places because overshadowed by strong snow returns. However, the water cloud regions, i.e. the low depolarization blue regions, stand out very well in the depolarization map. Actually, we see two water cloud layers with ice crystals in between although the second layer is masked by the first one on the east side of the map. Of further interest here is the spatial variability of the airborne snow concentration.

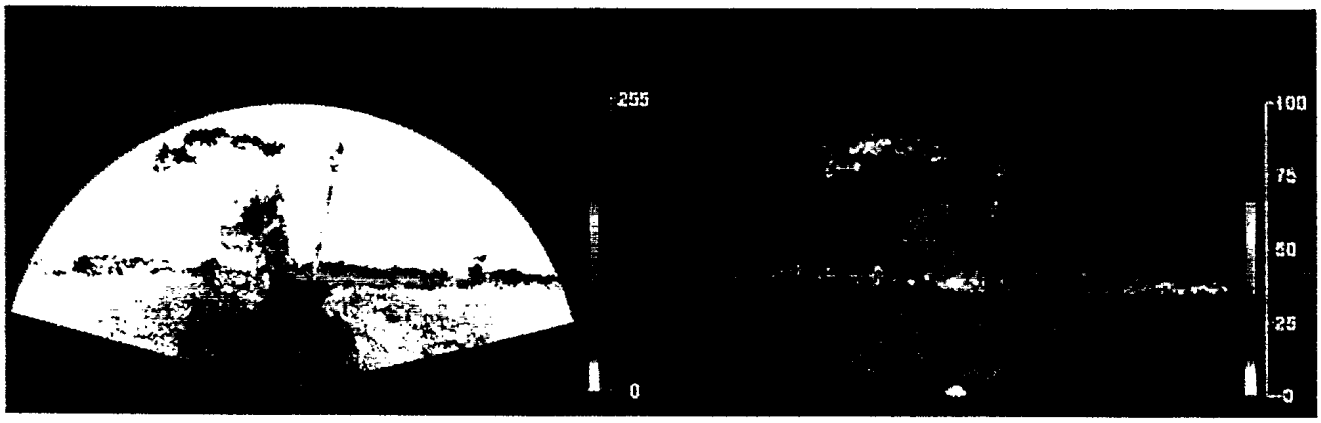

Figure 5. Color-coded elevation-versus-range backscatter (left) and depolarization ratio (right) maps obtained on 10 April 99 at 21:34 UTC. Scan plane is oriented east-west with the east or mountain side to the right. Radius of scan is 1.5 km. Backscatter scale is logarithmic and in arbitrary units; depolarization scale is %. Extended regions of 100% depolarization are default values for negligible signal strength.

The results of Figs. 3 to 5 are good examples of the information that can be derived from lidar returns even before quantitative retrieval is attempted. We have observed many cases with oriented crystal plates, other cases that showed a wavy structure of the cloud base, and at least one case also documented by the doppler radar that revealed a down slope flow in the opposite direction to the dominant wind aloft. This information coupled with the meteorological radar data will certainly contribute to a more complete picture of the prevailing local cloud physics conditions during MWISP. Much of our observations are complementary to radar measurements; for instance, radars

have difficulty making out small cloud droplets, especially in a situation such as depicted in Fig. 5 where ice crystals returns probably swamp everything else in the radar picture.

3.3. Retrieved Droplet Size and LWC

Our sequential FOV measurement method requires that the lidar pointing direction remain fixed during the scanning of the FOVs. The preferred measurement scenario used in the MWISP experiment, i.e. one that allowed the greatest cloud penetration depth, was to point the lidar in the vertical direction and make burst measurements every minute for periods of about 1 hour. For the retrieval results reported here, we integrated over 19 consecutive FOV sequences out of the 31 that constitute a burst. The solutions are calculated independently for each burst, no information from preceding or following bursts is assumed.

The solutions for a sample 1-hour long period are shown in Fig. 6. Three color-coded time series maps are reproduced: the top one for the depolarization ratio in %, the middle one for the effective droplet diameter in μm, and the bottom one for the LWC in g/m^3. The horizontal axis is time of day and the vertical axis is altitude expressed in μs (1 μs = 150 m) for a total range of 0-900 m. Each vertical stripe of the maps represents results from one burst and the width of the stripes is equal to the 1-min interval between the bursts. The solutions start at 200 m because the small FOVs are out of focus at closer ranges.

The depolarization map shows a clear water droplet cloud base and a light snowfall below. The conditions are relatively stable with the cloud base slowly descending from 750 m at the beginning of the period to 600 m at the end. The effective diameter is on the order of 20 μm in the cloud and 200-300 μm in the snow. The 300-μm value nears the upper limit of the retrieval method determined by the smallest resolvable FOVs and, therefore, the results of Fig. 6 may underestimate the true size of the precipitation crystals. The LWC averages about 0.1-0.2 g/m^3 in the cloud. For snow, the retrieved LWC plotted in Fig. 6 is not valid since the calculation method used to derive LWC from the extinction and diameter solutions assumes spherical shape and water density which are both obviously wrong for snow crystals.

It is emphasized that the solutions for each burst or vertical stripe in Fig. 6 are obtained independently of one another. Yet, the calculated solutions mapped in the middle and bottom panels of Fig. 6 show continuity. Therefore, our MFOV solution method gives consistent results and is not overly sensitive to measurement fluctuations. The solutions are noisier in precipitation than in cloud. This follows from greater signal noise because there are much fewer precipitation crystals than there are cloud droplets in the instantaneous lidar scattering volume.

A second example is given in Fig. 7 which shows similar maps as in Fig. 6 obtained in the same fashion but for a different 1-hour long period during which precipitation began to fall as mixed snow and rain and gradually evolved to a very light drizzle. This is clearly indicated by the depolarization map that shows, below cloud base, a ratio dropping from about 30% one third into the period to only a few percent at the end. The high depolarization at the very beginning of the period is not real but simply the default value for very low signal levels, the precipitation was insignificant there. On the other hand, the depolarization in the probed cloud depth is consistently low throughout the period indicating a predominance, in terms of lidar backscatter strength, of the water phase in the cloud itself.

The effective droplet size solutions give a diameter that fluctuates around 100 μm in the drizzle and 15-20 μm in the cloud. The LWC is near 0.1 g/m^3 in the cloud and slightly less in the drizzle. There is a thin blue line at the top of the LWC profile corresponding to very low LWC values. This results from a sharp break in the fading rate of the lowest FOV signal as it nears the detection threshold that is most likely due to an electronic artifact. Finally, the missing stripes in the solution maps are the results of a software glitch.

Both Figs. 6 and 7 show that the LWC profiles have a maximum some 50-60 m into the cloud. It is not possible to ascertain at this time whether the maximum is real or not except to observe that it is consistent throughout both periods and agrees with the measured relative strengths of the raw MFOV returns. More analysis will be carried out on all available data to investigate if this might be the result of a systematic bias of the solution method or measurement technique.

4. DISCUSSION AND CONCLUSION

Although the retrieved solutions of Figs. 6 and 7 are spatially and temporally continuous and give values in the expected ranges for these situations, they remain to be fully validated. The coordinated analysis of the MWISP

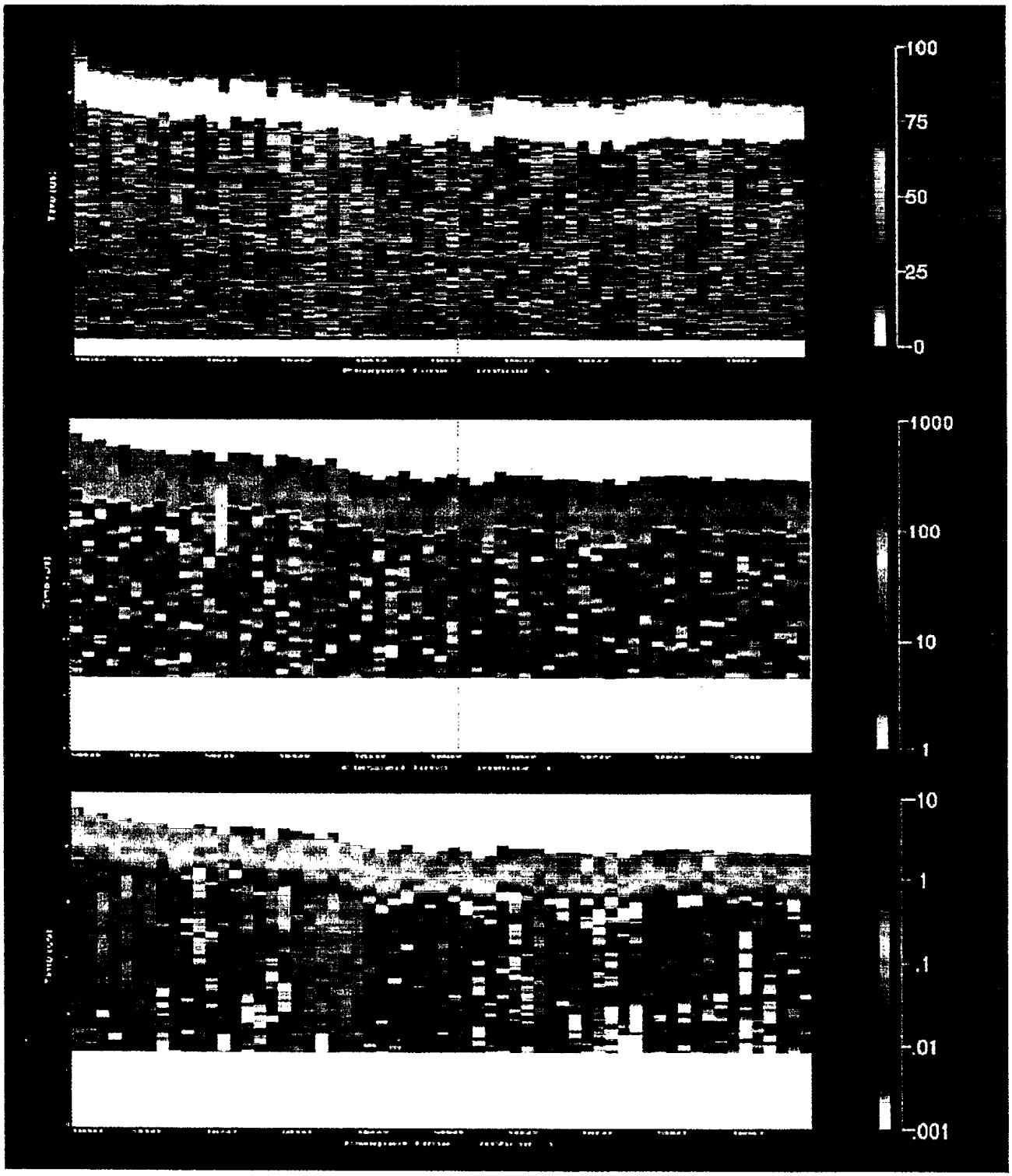

Figure 6. Color-coded altitude-versus-time maps of depolarization ratio (top), retrieved effective droplet diameter (middle) in μm, and retrieved LWC (bottom) in g/m^3 for a 1-hour long period beginning at 16:03 UTC on 10 April 99. Each vertical stripe corresponds to one lidar burst. Altitude is expressed in μs (1 μs = 150 m) for a total range of 0-900 m.

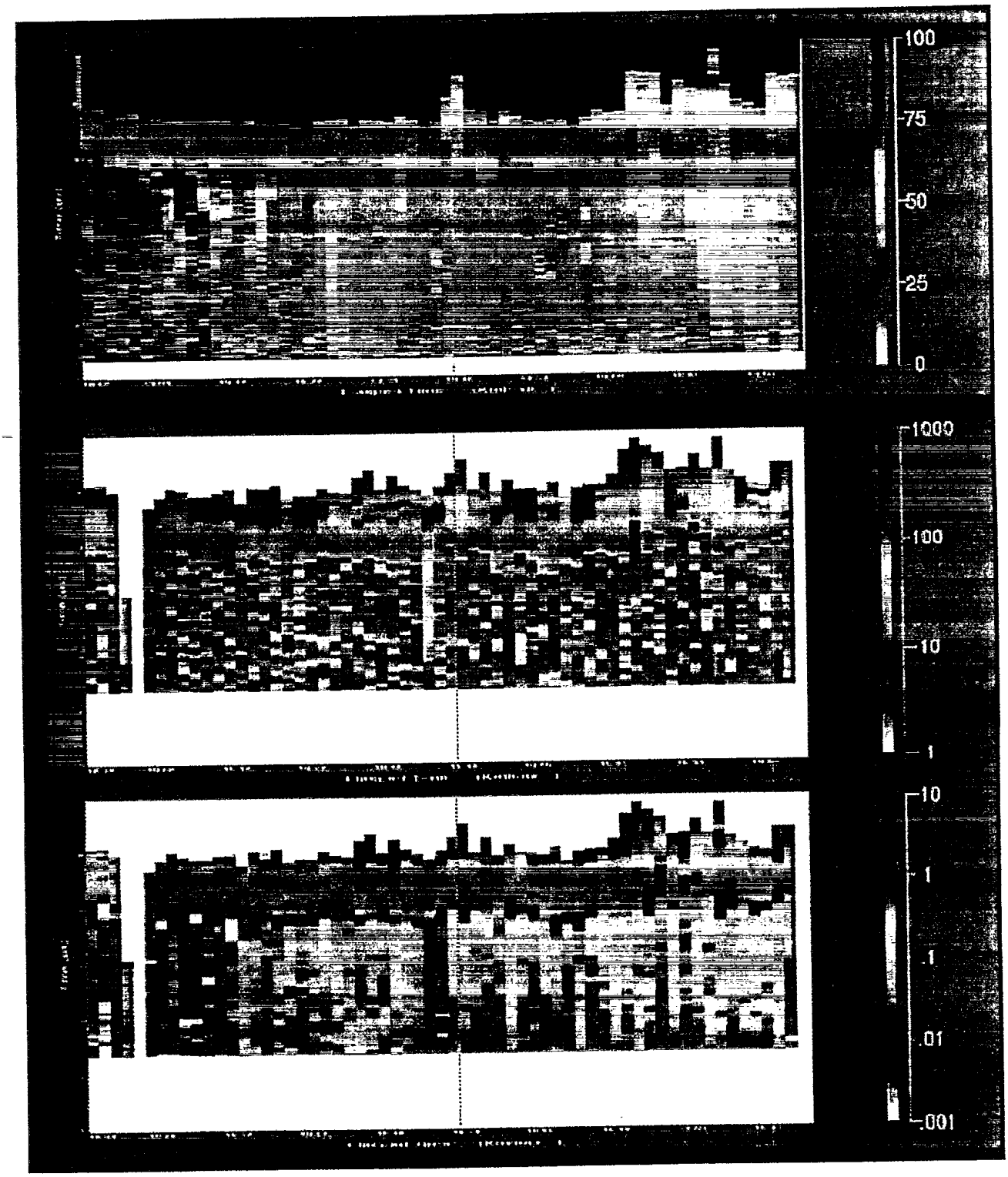

Figure 7. Color-coded altitude-versus-time maps of depolarization ratio (top), retrieved effective droplet diameter (middle) in μm, and retrieved LWC (bottom) in g/m^3 for a 1-hour long period beginning at 18:58 UTC on 14 April 99. Each vertical stripe corresponds to one lidar burst. Altitude is expressed in μs (1 μs = 150 m) for a total range of 0-900 m.

data from all deployed sensors will certainly contribute significantly to this need. However, we cannot expect to make detailed correlations because of the wide separation between the sensors compared with the variability of the conditions and the high resolution of the lidar solutions. Nevertheless, average values and broad spatial and temporal patterns should make useful validation tests.

The consistency observed in the solutions of Figs. 6 and 7 is a qualitative measure of accuracy but we can go one step further. The system constant C should remain just that, a constant, during the hour long measurement periods depicted in Figs. 6 and 7. The true system fluctuations come from the detectors sensitivity to local temperature and the shot-to-shot variations of the laser pulse energy. In normal operating conditions, these can account for oscillations in C of only a few percent, 10% at the most. In our solution method, we calculate a new constant C for every lidar burst based on the current burst data only, i.e. independently of the preceding and following returns and other inputs. In other words, the resulting variations in the calculated C over the hour long measurement periods are driven by burst-to-burst experimental fluctuations in the lidar returns. Since by eq. 6 α is proportional to C, we expect the errors on the retrieved extinction coefficient α to be of the same order as the errors on C. For all retrievals calculated to date, we find that C fluctuates by 30-40%. Hence, the accuracy of the detailed solutions of Figs. 2, 6 and 7 should approximate 30-40%. What will be the resulting effect on temporal and spatial averages derived from these solutions, we do not know for the moment but the MWISP analysis will certainly help quantify this.

In conclusion, the results of Figs. 3-7 show that the MFOV lidar can provide with reasonable accuracy detailed information on cloud/precipitation structure and microphysics. These data are directly applicable to the remote characterization of in-flight icing conditions. Of the needed parameters, only temperature is missing. The main drawback of the lidar approach is limited cloud penetration depth. Hence, there remains to determine how characteristic of the whole cloud deck are the first 150-300 m typically accessible to the lidar.

Acknowledgments

The measurements reported here were supported by NASA Glenn Research Center under Services Order Number C-77113-J. The authors gratefully acknowledge the able technical assistance of C. Bastille and G. Vallée.

REFERENCES

1. G. Fiocco and L.D. Smullin, "Detection of scattering layers in the upper atmosphere (60-140 km) by optical radar," *Nature* **199**, pp. 1275-1276, 1963.
2. J.D. Klett, "Stable analytical inversion for processing lidar returns," *Appl. Opt.* **20**, pp. 211-220, 1981.
3. L.R. Bissonnette and D.L. Hutt, "Multiple scattering lidar, " *Appl. Opt.* **29**, pp. 5045-5046, 1990.
4. D.L. Hutt, L.R. Bissonnette, and L. Durand, "Multiple field of view lidar returns from atmospheric aerosols," *Appl. Opt.* **33**, pp. 2338-2348, 1994.
5. *Applied Physics*, Volume B60, Number 4, April 1995.
6. L.R. Bissonnette, "Multiple-scattering lidar equation," *Appl. Opt.* **35**, pp. 6449-6465, 1996.
7. L.R. Bissonnette and D.L. Hutt, "Multiply scattered aerosol lidar returns: inversion method and comparison with *in situ* measurements," *Appl. Opt.* **34**, pp. 6959-6975, 1995.
8. G. Roy, L.R. Bissonnette, C. Bastille, and G. Vallée, "Estimation of cloud droplet size density distribution from multiple-field-of-view lidar returns," *Opt. Eng.* **36**, pp. 3404-3415, 1997.
9. G. Roy, L.R. Bissonnette, C. Bastille, and G. Vallée, "Retrieval of droplet-size density distribution from multiple-field-of-view cross-polarized lidar signals: theory and experimental validation," *Appl. Opt.* **38**, 1999 (in press).
10. L.R. Bissonnette and G. Roy, "Cloud measurements with a multiple-field-of-view, dual polarization lidar system," *Proc. of 19th International Laser Radar Conference*, edited by U.N. Singh and S. Ismail, NASA/CP-1998-207671/PT1, pp. 51-54, 1998.
11. G. Roy, L.R. Bissonnette, and C. Bastille, "Efficient field-of-view control for multiple-field-of-view lidar receivers," *Proc. of 19th International Laser Radar Conference*, edited by U.N. Singh and S. Ismail, NASA/CP-1998-207671/PT1, pp. 767-770, 1998.
12. L.R. Bissonnette and G. Roy, "Retrieval of extinction coefficient and effective droplet diameter from multiply scattered ground-based lidar returns," *Proc. Europto Series*, SPIE **2956**, pp. 86-94, 1996.
13. G.J. Kunz, "Transmission as input boundary value for an analytical solution of the single scatter lidar equation," *Appl. Opt.* **35**, pp. 3255-3260, 1996.

#512722